Diffraction Effects From Giant Segmented Mirror Telescopes

Mitchell Troy[a] and Gary Chanan[b]

[a]Jet Propulsion Laboratory, California Institute of Technology, Pasadena, CA, USA 91109
[b]Department of Physics and Astronomy, University of California Irvine, Irvine, CA 92697

ABSTRACT

Ultra-high contrast imaging with giant segmented mirror telescopes, will involve light levels as small as 10^{-9} times that of the central diffraction spike. At these levels it is important to quantify accurately a variety of diffraction effects, including segmentation geometry, intersegment gaps, obscuration by the secondary mirror and its supports, and segment alignment and figure errors, among others. We describe an accurate method for performing such calculations and present preliminary results in the context of the California Extremely Large Telescope.

Keywords: Telescopes, Segmented Mirrors, Adaptive Optics, Phasing, Diffraction

1. INTRODUCTION

One of the key scientific motivations for a diffraction-limited giant segmented mirror telescope, such as the proposed 30 meter California Extremely Large Telescope (CELT), is the potential for ultra-high contrast imaging, as for example in searches for planets outside the solar system. Mature planets, seen in reflected light, should in principle be seen at brightnesses of about 10^{-9} times that of the parent star at angular separations of 0.5 to 1 arcsecond; young planets, with an effective temperature of 600 to 800 K, should have relative brightnesses as high as 10^{-6} with angular separations of a few tenths of arcseconds (reference). Figure 1 shows that these parameters are consistent with the diffraction limit of a (circular) 30 meter telescope at a wavelength of a micron (and far more favorable than for a 10 meter telescope, for which the maximum contrast ratio beyond 0.2 arcseconds is 30 times higher).

If we are interested in imaging point sources in or near the wings of bright sources that are a million or more times brighter, then "diffraction limited" is a necessary but not sufficient condition, and a variety of diffraction effects, which under ordinary circumstances may be quite negligible, can assume a central importance. Additionally it follows that the calculation of such diffraction effects must be done quite accurately. Calculations of such high accuracy in the context of extremely large telescopes are not trivial, as can be seen from the following argument.

As usual the intensity distribution in the image plane is obtained from (the absolute value squared of) the Fourier transform of the aperture function. For a large Fast Fourier Transform of 4096 by 4096 elements (which must necessarily be complex), the aperture is sampled with a resolution of order 2 x 30 meters/4096 or 14 mm, where the factor of 2 is for the assumed underfilling of the array. This resolution is considerably cruder than is needed to resolve the intersegment gaps (estimated to be 4 mm for CELT) and barely adequate for the support cables for the secondary mirror (38 mm in diameter).

In the following (Section 2) we describe a mathematical framework - the grey pixel approximation - for calculating the relevant diffraction patterns with sufficient resolution and accuracy, without having to resort to extremely large FFT arrays. In Section 3, we demonstrate the accuracy of this approximation scheme, and in Section 4 we apply it to calculate the diffraction consequences of numerous effects of interest. Our conclusions are summarized in Section 5.

A complete treatment of diffraction-limited imaging from a ground based telescope must necessarily involve adaptive optics (AO). However, an AO system will do virtually nothing to reduce those diffraction effects resulting principally from amplitude variations (relative to a circular aperture). These effects include:

Further author information: M. Troy: mtroy@jpl.nasa.gov, G. Chanan: gchanan@galaxy.ps.uci.edu

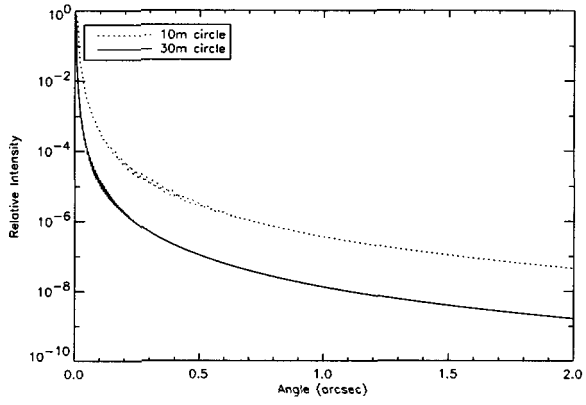

Figure 1. Diffraction limits for 10 and 30 meter circular telescopes at a wavelength of 1 μm and a Gaussian bandpass of 3% FWHM. [The finite bandpass smooths out the structure of these curves beyond about 0.5 arcsec.] Beyond about 0.2 arcsec the diffraction wings of the 30 meter telescope are 30 times lower than those of the 10 meter telescope.

- segmentation of the pupil outline
- intersegment gaps
- obscuration by the secondary mirror supports
- varying segment reflectivity

The second category of diffraction effects concerns those resulting from phase variations (relative to a perfectly flat wavefront). These effects include:

- segment piston/tip/tilt errors resulting from the primary mirror control system
- segment piston alignment errors
- segment tip/tilt alingment errors
- segment aberrations
- global radius of curvature (focus mode) error

In these latter cases, an AO system will reduce the phase errors and therefore the undesired diffraction effects to some extent. However, for the last four cases, which correspond to spatial scales of a segment diameter or less, we expect the improvement due to AO to be relatively small. [To see this, note that these effects are by definition not corrected by the telescope active control system, which - at three actuators for each of its 1080 segments - is in some sense the equivalent of a 3240 degree of freedom deformable mirror.]

For the case of primary figure errors resulting from the control system itself, the effective spatial frequencies are rather low (see discussion below), and as a result in this (single) case an AO system should effect a substantial improvement. In a future paper we will look more closely at the effect of AO correction on telescope aberrations; for now our treatment can be regarded as a worst case analysis.

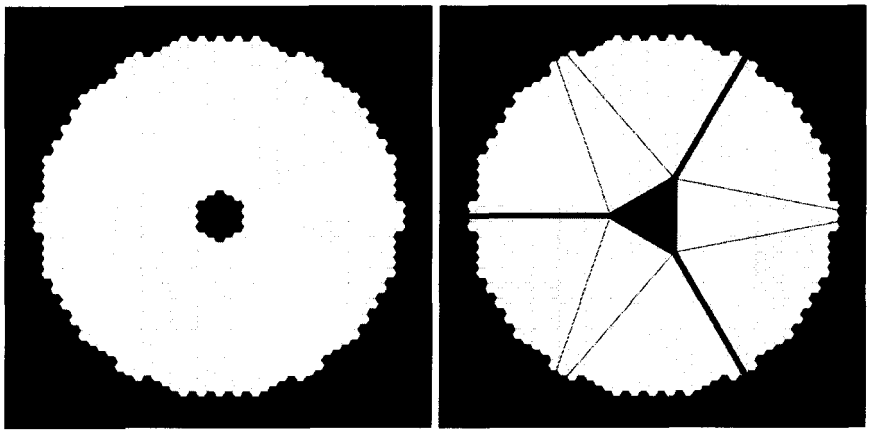

Figure 2. The proposed aperture for the 30 meter California Extremely Large Telescope (CELT), showing the segmentation geometry and the approximately circular outline (left). The figure on the right includes the typical obscuration due to the secondary mirror and its supports.

2. DESCRIPTION OF THE GREY PIXEL APPROXIMATION

As noted above, for a 30 meter telescope with FFT arrays of practical size, the bins or pixels in the aperture array are too small to represent faithfully the smallest features of interest (generally the intersegment gaps) in the true aperture. That is, if we color an aperture pixel black or white according to whether it is mostly in or mostly outside of a gap, the resulting map will be only a poor approximation of the actual gap structure of the primary mirror. However, one can do better (at least conceptually) by coloring each pixel near the gap an appropriate shade of grey according to what fraction of the pixel actually falls within the gap. A simple and straightforward procedure for the optimal shading - the grey pixel approximation (GPA) - is obtained as follows.

As usual we obtain the complex amplitude $\hat{f}(\vec{w})$ in the image plane from the Fourier Transform of the aperture function $f(\vec{\rho})$.

$$\hat{f}(\vec{w}) = \int\int e^{ik\vec{\rho}\cdot\vec{w}}\ f(\vec{\rho})\ \rho\ d\rho\ d\theta \tag{1}$$

Note that $f(\vec{\rho})$ is a complex function whose phase is the phase error (in radians) associated with the wavefront at ρ, and whose amplitude defines its intensity. Here $k = \frac{2\pi}{\lambda}$, $\vec{w}$ has circular coordinates (w, ψ) or rectangular coordinates (u, v) (in radians), and the absolute value squared of $\hat{f}(\vec{w})$ gives the intensity (per radian squared) in the image plane.

For a periodic array of identical primary mirror segments with centers at $\vec{\rho}_i$ we have

$$\hat{f}(\vec{w}) = \hat{h}(\vec{w}) \sum_i e^{ik(\vec{\rho}_i\cdot\vec{w})} \tag{2}$$

where $\hat{h}(\vec{w})$ is the complex amplitude in the image plane of a single segment centered at (0,0). We consider CELT with 1080 hexagonal mirror segments (see Figure 2a). Analytical expressions for $\hat{h}(\vec{w})$ for the five possible cases (depending on (w, ψ)) are given by Chanan and Troy.[1]

The hexagon side length enters the above formalism implicitly in two different places: once in defining the array of centers of the hexagonal pattern (for definiteness, we refer to the parameter in this role as a) and once in defining the physical size of the segments themselves (which we denote as a'). There is no a priori reason why we must have $a' = a$, and in fact if $a' < a$, then Eq. 2 represents an array of segments separated by gaps of

width $g = sqrt(3)(a - a')$. We can therefore write an analytical expression for $\hat{f}(\vec{w})$ corresponding to a perfect image, and take the inverse transform of this to obtain the aperture function. This aperture function is optimal in the sense that it will produce exactly the right image, including the correct effects of gaps. [To be precise, this function is exact in that it represents the correct intensity at the center of each pixel, but still approximate in the sense that in a real detector, the measured intensity is instead averaged over the area of the pixel.]

There are several subtleties to note when using this procedure:

1. The aperture function obtained in this way will be real (at least for a symmetric pupil), but it can go negative near the aperture boundaries. This does not cause any particular problems, however.

2. In the absence of aberrations or other obscurations, this procedure is exact in the sense that (by construction) it produces exactly the right image for a perfect wavefront. The approximate aspect of the grey pixel approximation comes about when (i) we obtain the complex amplitude by multiplying the amplitude obtained in this way by $e^{i\phi}$ where ϕ is the phase error (in radians) associated with an aberrated wavefront, or (ii) replacing the amplitude by 0 if the corresponding point on the wavefront is obscured, e.g. by the secondary mirror supports. Below we shall show that the errors associated by introducing these approximations can be reduced to an acceptable level.

3. Implementation of the grey pixel approximation is time consuming for a highly segmented mirror because of the necessity of evaluating the large number of phase factors in Eq. 2 for every pixel in the array. However, considerable computation time can be saved by:

   (a) exploiting the fourfold symmetry of the perfect aperture function, so that the phase factors only need to be calculated for 1/4 of the points in the array

   (b) noting that the imaginary part of the (perfect) complex amplitude must vanish and hence need not be calculated

   (c) utilizing various trigonometric identities to rewrite the generic phase factor in Eq.(2) so that it becomes:

$$\hat{f}(\vec{w}) = \hat{h}(\vec{w}) \sum_i cos(kx_i u) * cos(ky_i v) \tag{3}$$

   This in effect reduces the two-dimensional problem to two one-dimensional problems, with an accompanying large savings in computation time.

The net effect of the above three modifications is to reduce the calculation time for Eq. 3 to the point where it is comparable to the time required for the FFT, so that the grey pixel approximation only takes between 2 and 3 times the time required for the much cruder black-or-white pixel approach.

3. VALIDATION OF THE GREY PIXEL APPROXIMATION

A rigorous mathematical analysis of the grey pixel approximation is beyond our scope here, but we can nevertheless get a sense of its accuracy by means of the following approach. As we increase the number of bins in the FFT array, while keeping the aperture a fixed fraction of the overall size of the input array, the accuracy of the grey pixel approximation should increase as the sampling of small features, such as the intersegment gaps, improves. Therefore, the rate of convergence of (for example) the image profiles with increasing array size provides a measure of the accuracy of the approximation. To illustrate this we consider pure second order segment aberrations (focus and astigmatism, with no piston, tip, tilt or higher order aberrations) on a 1080-segment CELT. We consider rms surface errors of 100 nm in each of the three second order aberrations (or 173 nm total) - rather large compared to the effects we consider below - and array sizes for each of 1024, 2048, and 8192 (squared). [Note that there is no convergence issue in the absence of aberrations, since in that case the GPA is exact, independent of the size of the FFT array.] The corresponding radial profiles are presented in Figure 3a; note the excellent convergence within a radius of 2 arcseconds.

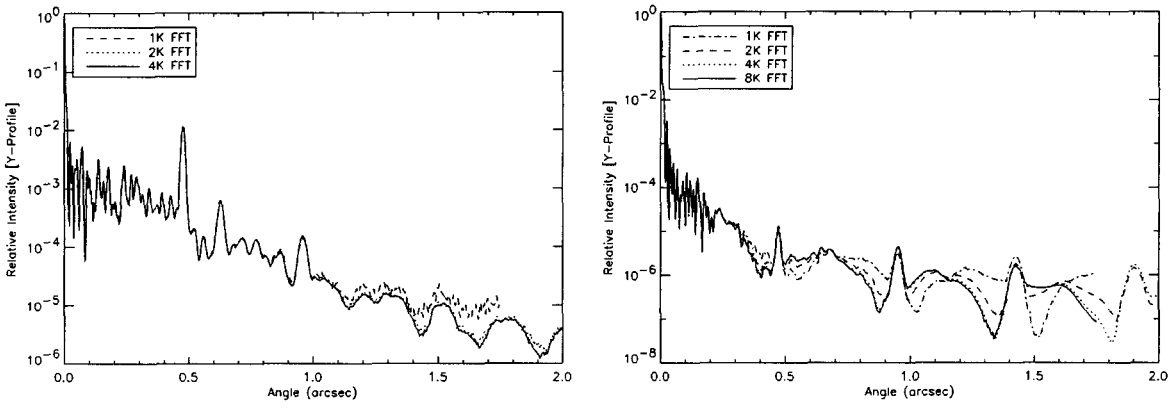

Figure 3. Left convergence of the grey pixel approximation for phase effects, in this case 100 nm each of the three second order surface aberrations. Within 2 arcseconds excellent convergence is obtained for an array of 4096 pixels on a side, but not for 1024 pixels on a side. Right convergence of the grey pixel approximation for amplitude effects, in this case the obscuration associated with the secondary mirror and its supports as shown in Figure 2b. Within 2 arcseconds excellent convergence is obtained for an array of 8192 pixels on a side, but not for 2048 pixels on a side. Note that these amplitude effects require about twice as many pixels as do the phase effects for comparable convergence.

For completeness we also examine the convergence of the grey pixel approximation for amplitude effects, to be specific those due to the presence of the secondary mirror and its supports. (see Figure 2b). These radial profiles are presented in Figure 3b. In this case the convergence is somewhat slower than for the phase effects; excellent convergence is still obtained, but it requires array sizes of 8192, not 4096, on a side. In the following calculations we use 4096 x 4096 transforms when no obscuration is present and 8192 x 8192 when the obscuration is present. The results are generally presented as radial image profiles. In cases where the is a preferred orientation, e.g. diffraction effects associated with intersegment gaps, or secondary mirror supports, we present the profiles along the X or Y axes (parallel or perpendicular to the segment edges), generally whichever shows the most dramatic variation. For cases in which there is no obvious preferred orientation, e.g. segment aberrations or reflectivity variations, we present azimuthally averaged profiles.

4. CALCULATION OF DIFFRACTION EFFECTS

4.1. Amplitude Effects

1. Segmentation effects

   In its current design the CELT primary mirror consists of 1080 hexagonal segments, 0.5 meters on a side, in a circularized arrangement (Figure 2a), with the 19 central segments missing (and excluded from the above total). Figure 4a shows the theoretical image (1 arcsec by 1 arcsec) of a point source (logarithmic plot) produced by CELT at a wavelength of 1 micron; it exhibits the characteristic hexagonal symmetry associated with this design. In Figure 5 we present image profiles in the x direction (parallel to the intersegment edges) corresponding to this case. For comparison we also show the profiles corresponding to an uncircularized arrangement of 1122 segments in 19 hexagonal rings (again with the central 19 segments missing and excluded from the total), and the profiles for a circular telescope 30 meters in diameter. The profiles for the segmented telescopes were calculated in the GPA, the circular profile is exact. To miminize the extremely high spatial frequency variations associated with monochromatic images for the segmented cases, these profiles have been calculated assuming a wavelength bandpass of 3% FWHM of the central wavelength. Note that the diffraction effects for the circularized CELT are considerably milder than for the uncircularized version, and tend to be intermediate between the uncircularized case and a true circle. [The diffraction effects in other directions are more modest and are not shown.] For the rest of this work we only consider the circularized CELT design.

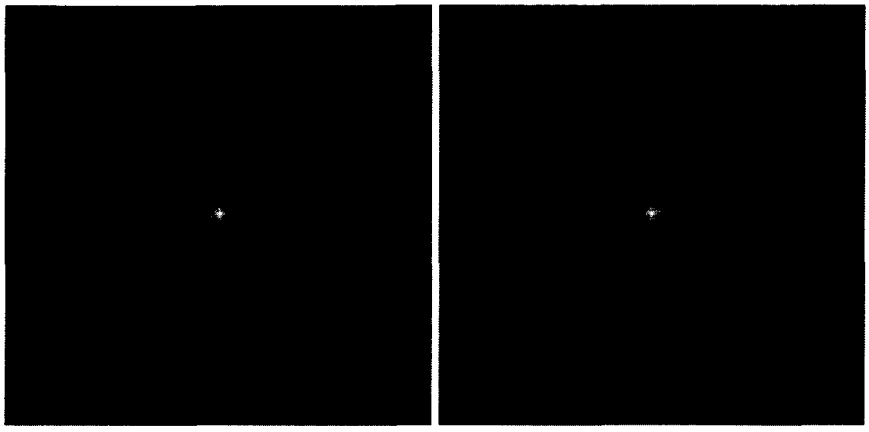

Figure 4. Left logarithmic image for CELT (1 arcsec by 1 arcsec) showing the characteristic hexagonal symmetry. No intersegment gaps or obscuration is included. The figure on the right shows the readily apparent effects of the obscuration due do the secondary mirror and its supports (and also including the relatively minor effects due to intersegment gaps).

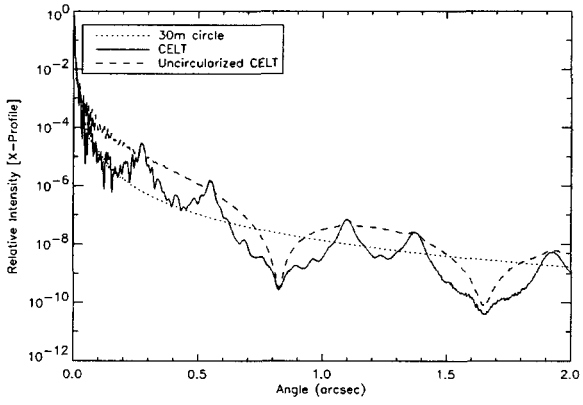

Figure 5. Image profiles for a circular 30 meter telescope, for CELT with the nominal circularized design (Figure 2a; see also Figure 4a), and for an uncircularized CELT with 1122 segments in 19 rings. For the latter two, the profiles are in the direction parallel to the segment edges. In this direction, the circularized CELT backgrounds are virtually always lower than for the uncircularized CELT, often significantly so. Differences between the curves in other directions are much more modest.

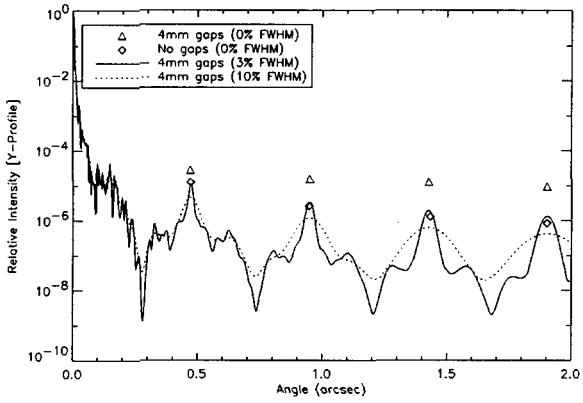

Figure 6. CELT radial profiles in the Y-direction (perpendicular to the segment edges) for various bandpasses showing the effects of 4 mm gaps. The zero gap case (at zero bandwidth) is also shown for comparison. Note that the gap-related features at intervals of 0.5 arcseconds are strongly attenuated as the bandpass is increased.

2. Intersegment gaps

   We next consider the effects of non-reflective gaps between segments; the expected gap width is of order d = 4 mm. In Figure 6 we present image profiles in the y-direction corresponding to gaps of this size, for bandpasses of 0, 3% , and 10% FWHM, all centered at 1 micron. [The effects of the gaps are much smaller in the x-direction (not shown) which runs parallel to the gaps.] Profiles from a zero-gap telescope are also shown for comparison. As usual, since the GPA was used, the results are essentially exact. The finite bandpass calculations were performed simply by superposing images for wavelengths spaced every 4 nm (?) from 3 sigma below to 3 sigma above the central wavelength. Since the image scale was kept constant while the wavelength was varied, the scale (in meters per bin) in the aperture plane had to be varied correspondingly.

   For monochromatic images, the gaps produce a series of point like features spaced at intervals of 0.5 arcseconds (2 λ/segment diameter). [For clarity only the peaks of these features are shown in the Figure.] The envelope of these point like features is of order one arcminute (λ/gap size) in width, and so their intensity falls off extremely slowly; the peak heights are of order 10^{-5} of the central peak within this envelope. Because of the factor $e^{ik\rho}$ in the Fourier Transform, these features smear out radially for finite bandwidths, where the degree of smearing increases both with the bandwidth and with the radial distance from the center of the image. Although the 4 mm gaps for zero bandpass produce features that are as much as an order of magnitude larger than for the zero gap case, for a 3% bandpass these features are no larger than for the zero gap case. [There are features at intervals of 0.5 arcseconds even without gaps because the hexagonal shape of the segments is still apparent at the inner and outer boundary of the aperture. For a 10% bandwidth these features are actually lower than for the zero gap, zero bandpass case.

3. Obscuration by the secondary mirror and supports

   Figure 4b shows a typical obscuration associated with the CELT secondary mirror and its supports.[2] The blockage consists of an equilateral triangle 7 meters on a side, three radial compression members 46 cm in cross section, and six non-radial cables 38 mm in cross section attached to the triangle vertices as shown. As a result of the variety of spatial scales, this structure scatters light over a broad range of angular scales in both the x and y directions. Figure 7 shows the X and Y image profiles with and without the obscuration. The effects are substantial - in places raising the background by two orders of magnitude or more. The increase below 0.5 arcseconds occurs principally in the Y direction, because it is associated

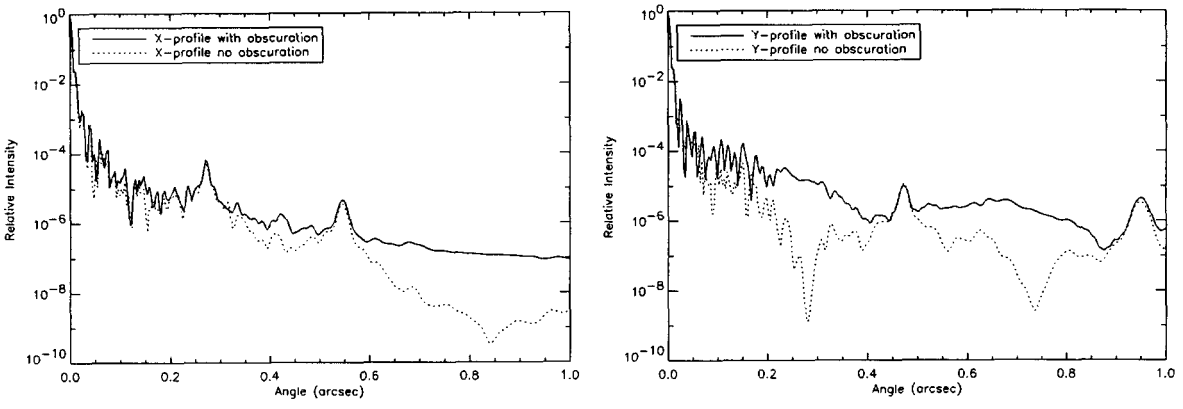

Figure 7. CELT radial X (left) and Y (right) profiles with and without obscuration showing the substantial increase due to the secondary mirror and its supports. The strong increase in the Y-profile background below 0.5 arcseconds is due to the compression members (46 cm in diameter) which support the secondary and run along the X axis.

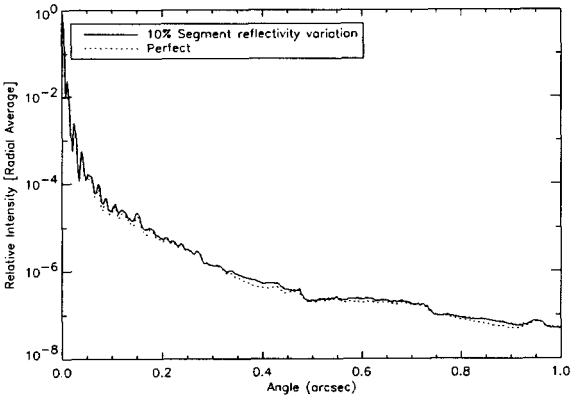

Figure 8. Azimuthally averaged CELT radial profiles for a 10% reflectivity variation from segment to segment. This profile is barely distinguishable from that of a uniform aperture.

with the larger member, which runs parallel to X.

Unlike the gap effects, these obscuration effects are not significantly reduced as the bandpass is increased.

4. Varying segment reflectivity

   Experience with the Keck telescopes shows that at any given time, the segment to segment variation in reflectivity for a given telescope may be of order 5% (rms) (reference). Variations of this size should have very little effect on the wings of the telescope diffraction pattern. To see this we considered an aberration-free CELT mirror, including the intersegment gaps and obscuration, but with 10% variation in segment reflectivity. The resulting image profiles are shown in Figure 8 for a 3% bandwidth. Even for these exaggerated reflectivity variations, the diffraction consequences are clearly small; the radially averaged profile is difficult to distinguish from the perfect reflectivity case.

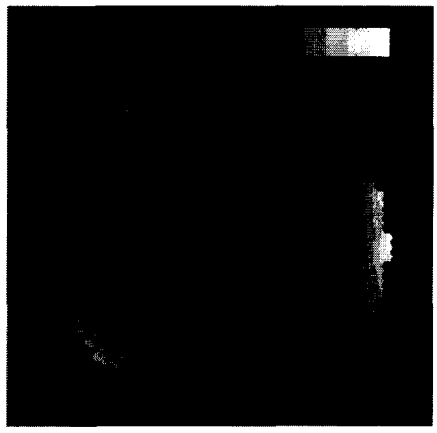

Figure 9. Aperture function for typical ACS noise, assuming a sensor noise of 1 nm rms. The corresponding actuator noise (roughly equal to the surface error) is 20 nm. Because of the low spatial frequency associated with aberrations of this type, these effects should be strongly attenuated by the adaptive optics system and thus are not considered further in this work.

4.2. Phase Effects

1. Segment piston/tip/tilt errors resulting from the control system

   As described elsewhere[2] for giant segmented mirror telescopes, significant wavefront errors can result from "control noise," i.e. the sensor noise propagated through the control matrix into the segment actuators. For CELT the actuator noise (to a first approximation equal to the corresponding surface error) will be about 20 times the sensor noise. The design goal for CELT sensor noise is 1 nm - a significant improvement over the nominal Keck value of 6 nm. Here we assume the optimistic value of 1 nm sensor noise or 20 nm surface error.

   Although these wavefront errors are large, they fortunately tend to be of fairly low spatial frequency (a typical control-induced wavefront error is shown in Figure 9), and as a result, should be largely canceled out by the adaptive optics system. Therefore, in the following, we ignore these large, low spatial frequency wavefront errors and instead focus our attention on the high spatial frequency residuals which are expected to be present after the cancellation of the low order effects by the AO system. Our experience to date with Keck provides useful estimates of these latter quantities. Specifically, these estimates come from the residual errors from the Keck alignment procedures in both piston and tip/tilt. All errors include the effects of measurement uncertainty. The piston errors include the high spatial frequency components of the control system errors (corresponding to spatial scales of a segment. The tip/tilt errors include control system errors at all spatial frequencies, and are thus conservative.

2. Segment piston errors

   At Keck we routinely reduce segment piston errors to 30 nm with the so-called broadband algorithm[3] but experiments with a narrowband algorithm, which is only slightly more time-consuming, have attained 10 nm.[4] Since both procedures phase all segments in parallel, we assume that we will be able to attain 10 nm for CELT as well. Figure 10 shows that piston errors of this magnitude produce a radial image profile which is barely distinguishable from that of a perfect mirror.

3. Segment tip/tilt errors (uncorrelated)

   At Keck segment typical segment tip/tilt errors, expressed as Zernike polynomials of the surface (not the wavefront) are 20 nm rms.[5] As noted above, these values are conservative in that they include errors from the control system as well as those from the measurement process; arguably it is only the latter

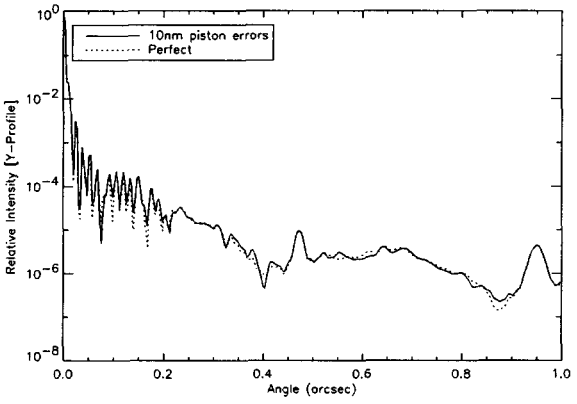

Figure 10. Azimuthally averaged CELT radial profiles for piston errors of 10 nm (surface, rms), about equal to the best Keck phasing results.

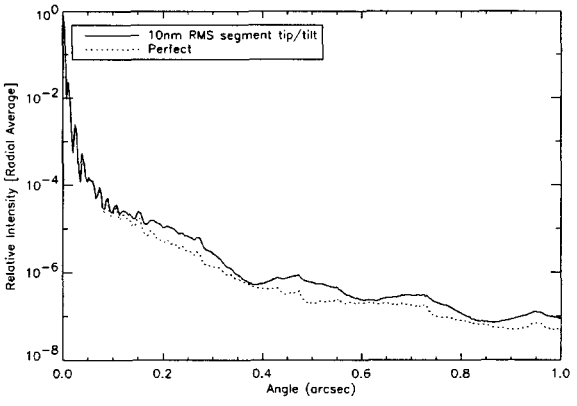

Figure 11. Azimuthally averaged CELT radial profiles for segment tip/tilt errors of 10 nm (surface Zernike coefficients, equal to angular errors on the sky of 0.008 arcsec (one-dimensional, rms), about a factor of 2 better than the best Keck tip/tilt alignments.

that are a concern here. Again, since the tip/tilt alignment process aligns all segments in parallel, it is reasonable to assume that similar numbers will apply to CELT, but to keep things parallel to the above piston errors analysis, we assume a more aggressive 10 nm tilt error (in each dimension). Figure 11 plots the radial profiles corresponding to these tip/tilt errors for a 3% bandwidth. Note that tip/tilt errors have significantly more effect on the image profiles than do piston errors; the difference is probably due to the higher effective spatial frequency of these errors, and to the fact that there are two tip/tilt degrees of freedom, compared to the one for piston. This Figure suggests that while current piston alignment techniques are probably adequate for CELT or other giant segmented mirror telescopes, it would be worth improving the tip/tilt alignment by a factor of several.

4. Segment aberrations

At Keck the rms segment surface error is 40 nm. These errors are dominated by second order aberrations - focus and astigmatism. Several improvements are planned to reduce these errors for CELT.[2] If these

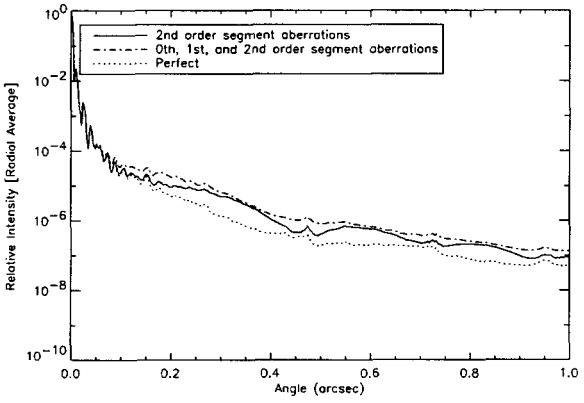

Figure 12. Azimuthally averaged CELT radial profiles showing the effects of 10 nm (rms) aberrations in each of the three second order terms, as well as the cumulative effects of these and the 0th and 1st order effects considered in Figures 10 and 11.

errors scale as the square of the segment diameter, then the above numbers correspond to about 7 nm surface errors in each of the three second order Zernike aberration terms. To be conservative we round these up to 10 nm each. We assume that the AO system will have little effect on these figure errors because of the high spatial frequencies involved.

Figure 12 shows the radial profiles associated with the above segment figure errors and also the corresponding profiles for the combined effects of piston, tip/tilt, and segment figure errors of the above magnitudes. Note that of these three aberrations, tipt/tilt are the most significant.

5. Global radius of curvature (focus mode) error

   A focus mode or global radius of curvature error occurs when the central rays from all segments intersect at a single point along the optic axis which does not correspond to the focus of the individual segments.

   A focus mode error is a concern for two reasons: (1) Focus mode is the most poorly controlled mode of the active control system,[2] and (2) the highly periodic nature of the resulting wavefront error can lead to sharp features in the image plane. In this case we cannot neglect the effect of the AO system (or even of a much lower bandwidth telescope focus control). In general the AO system or focus loop will approximate the existing focus mode with true focus (secondary despace) leaving "differential focus mode" - i.e. a common focus error on each segment, and producing a scalloped wavefront in collimated space. The rms global and differential focus mode errors are related by:

   Equation [Equation 3]

   Note that the ratio of differential to global focus mode varies as the inverse of the number of segments in the array (???). Preliminary analysis of the CELT active control system[2] suggests that the typical size of the focus mode error will be xx nm or less, corresponding to yy nm of differential focus mode. This latter number is sufficiently small that the effect in the image plane (not shown here) is virtually undetectable.

5. SUMMARY

The grey pixel approximation is an accurate and useful computational tool for evaluating the diffraction consequences of a large variety of effects which can potentially limit ultra-high contrast oberving with 30 meter class telescopes. Of all of the diffraction effects considered in this work, those associated with obscuration by the secondary mirror and its supports are by far the most significant within one arcsecond of the center of the image. Although intersegment gaps produce a large number of point like features at about 10^{-5} of the central

diffraction spike, these are rapidly attenuated as the bandwidth is increased. Segment phase errors, assuming levels of accuracy comparable to what can be achieved today with Keck, and variations in segment-to-segment reflectivity should have negligible diffraction consequences, but segment tip/tilt alignment and segment image quality (again scaled from Keck) should probably be improved by a factor of several for optimal high contrast imaging.

In a future paper we plan to extend this analysis to treat coronagraphic observations (see for example reference).

ACKNOWLEDGMENTS

This research was carried out in part at the Jet Propulsion Laboratory, California Institute of Technology, and was sponsored by the California Institute of Technology and the National Aeronautics and Space Administration.

REFERENCES

1. G. A. Chanan and M. Troy, "Strehl ratio and modulation transfer function for segmented mirror telescopes as functions of segment phase error," *Applied Optics* **38**, pp. 6642–6647, Nov. 1999.
2. J. E. Nelson and et. al., "California extremely large telescope conceptual design for a thirty-meter telescope," CELT Report No. 34, University of California, California Institute of Technology, Santa Cruz, CA, 2002.
3. G. A. Chanan, M. Troy, F. G. Dekens, S. Michaels, J. Nelson, T. Mast, and D. Kirkman, "Phasing the mirror segments of the Keck Telescopes: the broadband phasing algorithm," *Applied Optics* **37**, pp. 140–155, Jan. 1998.
4. G. A. Chanan, C. Ohara, and M. Troy, "Phasing the mirror segments of the Keck telescopes ii: The narrow-band phasing algorithm," *Applied Optics* **39**, pp. 4706–4714, Sept. 2000.
5. M. Troy, G. A. Chanan, E. Sirko, and E. Leffert, "Residual misalignments of the Keck telescope primary mirror segments: classification of modes and implications for adaptive optics," in *Proc. SPIE Vol. 3352, p. 307-317, Advanced Technology Optical/IR Telescopes VI, Larry M. Stepp; Ed.*, **3352**, pp. 307–317, Aug. 1998.